nature physics

ARTICLES

https://doi.org/10.1038/s41567-021-01244-w

Check for updates

Free electron to electride transition in dense liquid potassium

Hongxiang Zong[1,2], Victor Naden Robinson[2,3], Andreas Hermann[2], Long Zhao[1]✉, Sandro Scandolo[3], Xiangdong Ding[1] and Graeme J. Ackland[2]✉

At high pressures, simple metals such as potassium have a rich phase diagram including an insulating electride phase in which electrons have a localized, anionic character. Measurements in the liquid phase have shown a transition between two states, but experimental challenges have prevented detailed thermodynamic measurements. Using potassium as an example, we present numerical evidence that the liquid–liquid transition is a continuous transformation from free electron to electride behaviour. We show that the transformation manifests in anomalous diffusivity, thermal expansion, speed of sound, coordination number, reflectivity and heat capacity across a wide range of pressures. The abnormalities stem from a significant change in the local electronic and ionic structure. Although primarily a pressure-induced phenomenon, there is also a thermal expansion anomaly. By establishing the electride nature of the high-pressure liquid phase, we resolve the long-standing mystery of how a liquid can be denser than a close-packed solid. Our work is relevant for high-pressure thermodynamic properties of all alkali metal liquids.

Phase transitions are defined by discontinuous changes in properties of the material in question. In crystalline structures, they are typically associated with a change in symmetry, as well as a discontinuity in the lattice parameters and density. In magnetic transitions, the spontaneous magnetization drops to zero, and by definition, it cannot become negative. The meaning of a 'second-order' phase transition has evolved since Ehrenfest's original definition, namely, a 'discontinuity in the second derivative of free energy'. Nowadays, any divergent thermodynamic property is regarded as an indicator of a second-order transition. A final category of 'continuous' or 'infinite-order' transitions exists, which break no symmetries. In a liquid–liquid transition, there is no symmetry change, and a first-order transition is possible via a volume discontinuity. Such a transformation is typically (but not always) driven by a change in bonding character. An example is phosphorus, where a molecular liquid comprising tetrahedral P_4 molecules changes to a polymeric form[1]. Others include the molecular–atomic transition in hydrogen[2–5], superfluid helium[6] and the transition in water where the coordination rises from 4 to 8, mimicking the transition from the open ice I_h structure to the denser ice VII[7–12]. Examples of electronic changes with less obvious effects on bonding are the *f*-electron delocalization in liquid cerium[13] and the spin collapse in iron-rich silicate melts[14,15]. Often, these transitions are described as a two-state system: a first-order transition sees a finite fraction of particles switch between states, while in a continuous transition, the fraction of particles in each state varies continuously.

The electronic change underlying the liquid–liquid transition in alkali metals is not immediately obvious: these elements are the best examples of free-electron metals, with simple body-centred cubic (bcc) crystal structures. Under pressure, however, they have been observed to have a series of complex crystal structures, associated with a drop in the melting point, reduced conductivity and even insulating phases[16–19], including the discovered elemental electride (electrides have localized electrons at non-nuclear positions)[17]. This is related to a pressure-driven transformation from free electron to electride behaviour[20]. This is an electronic change; however, with two distinct types of bonding, it offers the possibility of a first-order transformation between two types of liquid. Alternatively, a continuous transition is possible, where the electride sites' proportion steadily rises from zero. The locations and signatures of any such transitions (if they exist) are not known. Electrides also exist at ambient pressure, often formed involving alkali metals in both crystalline and non-crystalline ionic salts[21,22]. Some exhibit exotic superconductivity or Mott insulator transitions[23,24], and due to their localized electron, they find applications in catalysis[25,26]. Recent computational machinery has been developed for the systematic prediction of stable electride structures[27].

Although the electronic and structural properties of crystalline alkali metals at different pressures have been studied in great detail, their liquid phases under high pressure are much less investigated[19,28,29] and not without controversy, for example, the liquid–liquid transition in cesium[30–33]. Experimental measurements of the macroscopic thermodynamic properties of alkali metal melts have proven to be an insurmountable challenge due to their high reactivity. A few studies have suggested structural transformations affecting the short-range order, resembling those reported in solids[19,33]. Ab initio molecular dynamics (AIMD) simulations were applied in high-pressure studies of the structural features of liquid alkali metals, reporting tetrahedral clustering of nearest neighbours in liquid lithium at a pressure of 150 GPa (ref. [34]), a possible metal–non-metal transition in liquid sodium[35], a Widom line crossing in rubidium[36] and abrupt coordination changes in cesium[37]. AIMD simulations on liquid potassium reveal a drop in coordination number from 14 to 8–10 under pressure[38], an effect also seen in other alkalis[37]. A major caveat in studying liquids with AIMD is the small system sizes: a liquid has some short-ranged structure, typically out to the 3rd or 4th neighbour shells; when looking for a structural phase transformation, these must be correctly described, unaffected by periodic boundary conditions.

[1]State Key Laboratory for Mechanical Behavior of Materials, Xi'an Jiaotong University, Xi'an, China. [2]Centre for Science at Extreme Conditions and School of Physics and Astronomy, The University of Edinburgh, Edinburgh, UK. [3]The 'Abdus Salam' International Centre for Theoretical Physics, Trieste, Italy. ✉e-mail: zhaolongxjtu@gmail.com; gjackland@ed.ac.uk

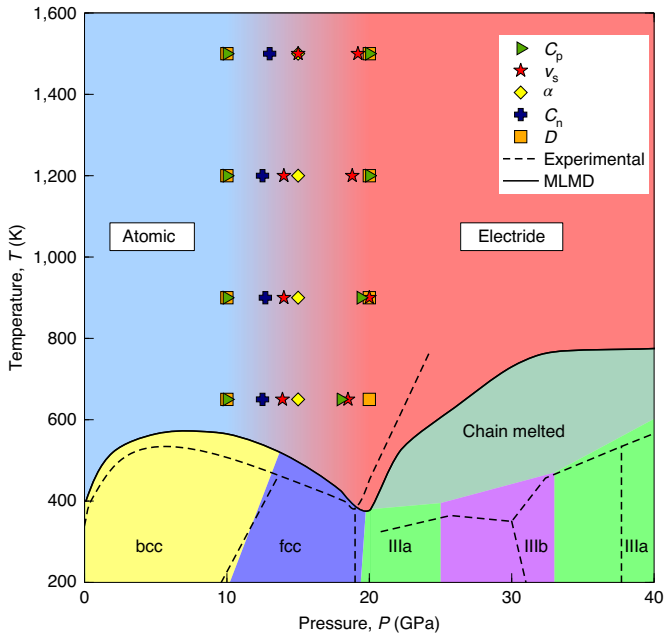

Fig. 1 | Phase diagram of potassium from MLMD simulations. The colours denote stability regions of phases as labelled. The dashed lines are experimental phase boundaries (solid–solid, solid–chain melt and solid–liquid) taken from McBride et al.[50]. The points in the liquid region show maxima and minima in heat capacity C_p and speed of sound v_s, minima in thermal expansion α, and maxima in high-coordination environments ($C_n > 15$; Supplementary Figs. 10 and 11) and boundaries of the plateau of diffusivity D.

Here we present an atomistic simulation of liquid potassium using a machine learning potential approach based on AIMD across a wide range of pressures and temperatures. This method allows our simulations to extend well beyond the short-range order in liquids, eliminating finite-size effects (Supplementary Fig. 1). We detect a range of thermodynamic and dynamic anomalies in the region of pressures between potassium's melting curve maximum and the appearance of electride solids[20] (10–20 GPa), which are mostly independent of temperature. Going back to the AIMD simulations, we relate these anomalies to changes in the electronic structure that suggest a continuous transition from a free-electron-like metal to an electride liquid.

Interatomic potential. The potential for potassium used in this work was derived by fitting to ab initio configurations of a range of high-pressure phases[20,39,40]. It has been shown to reproduce the entire high-pressure phase diagram with remarkable fidelity (Fig. 1), including both free electron and electride solids. Comparison of the properties calculated on small cells using AIMD and using the potential shows good agreement (Methods and Supplementary Note 1), which allows us to use it on larger cells and longer-time simulations.

Theory of partial electride liquid. Our central idea in understanding these results is that the liquid structure can be modelled as a mixture of two distinct electronic states, the low-pressure 'atomic' state and a high-pressure 'electride' state where electrons are localized in interstitial pockets. Mixing models with different complexities[41–43] are discussed in Supplementary Note 3. Different models give slightly different results, but all the mixing models display anomalies in heat capacity, thermal expansion and compressibility. Crucially, peaks associated with these anomalies do not fall in the same place. Specifically, the heat capacity maximum is at the lowest pressure, compressibility maximum at the highest pressure and

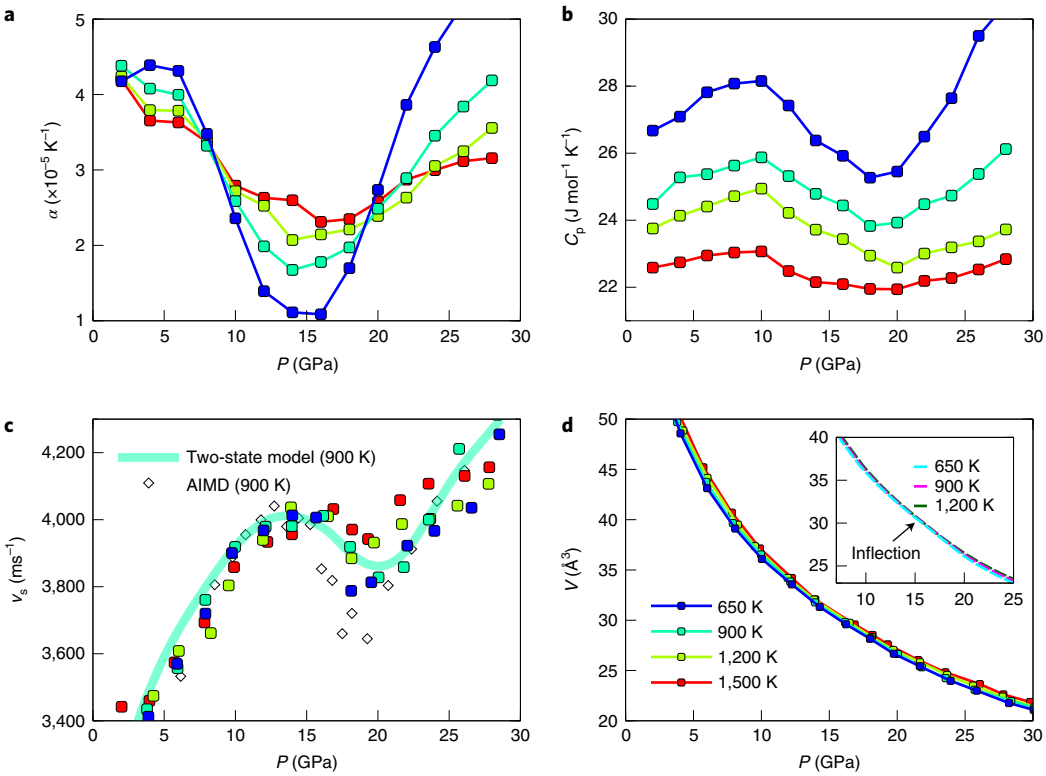

Fig. 2 | Thermodynamic quantities of liquid potassium, shown as a function of pressure for selected temperatures. a, Thermal expansivity α. **b**, Heat capacity C_p (excluding the electronic contribution; Supplementary Fig. 17). **c**, Speed of sound v_s (open diamonds show AIMD data at 900 K; cyan line shows the thermodynamic two-state model (Supplementary Note 3) fitted to the MLMD data at 900 K). **d**, Equation of state $p(V)$ (inset shows the AIMD data). Different colours of the solid symbols and lines represent different temperature data, as described in **d.**

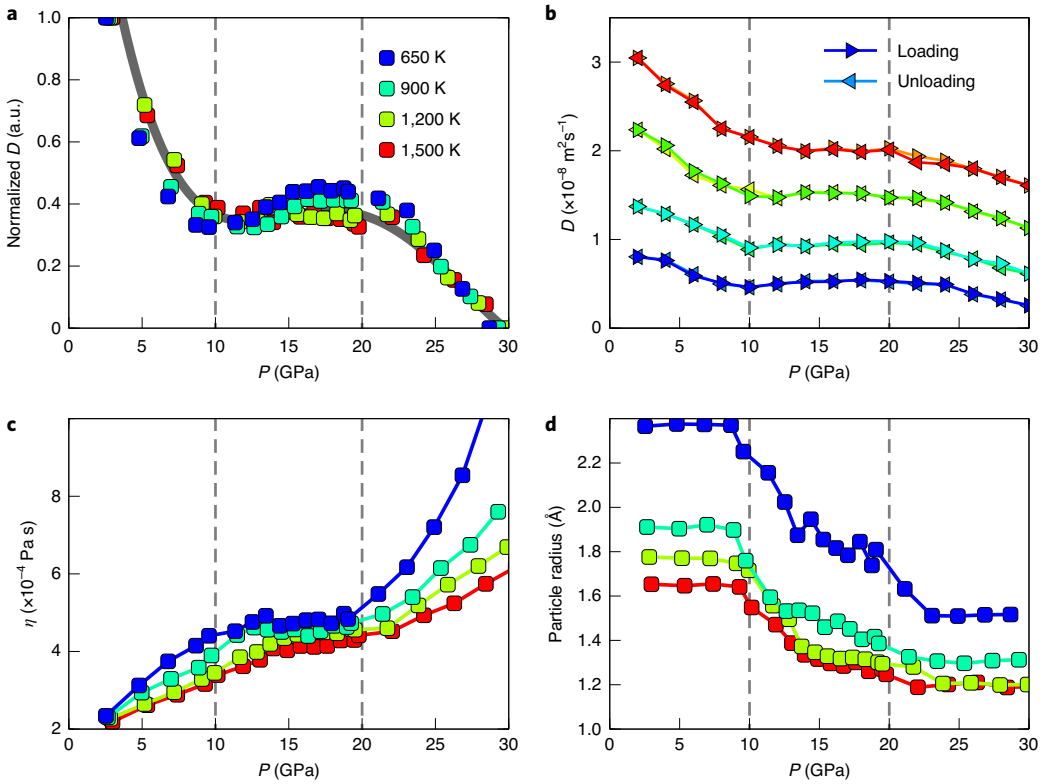

Fig. 3 | Dynamical properties of liquid potassium from MLMD simulations. a, Normalized diffusion constant versus pressure for selected temperatures: the solid line is a guide to the eye of the data collapse onto a single, T-independent curve once normalized as $D_{\mathrm{norm}} = \frac{D(P)-D_{\mathrm{min}}}{D_{\mathrm{max}}-D_{\mathrm{min}}}$. **b**, Absolute diffusion constants $D(P, T)$ from a series of calculations showing an absence of hysteresis on increasing and decreasing pressure. **c**, Viscosity μ calculated using the Green–Kubo stress fluctuation approach. **d**, Effective atomic radii R derived from μ by inverting the Stokes–Einstein relationship. Different colours of the solid symbols and lines in all panels represent different temperature data, as described in **a**.

thermal expansion dip at an intermediate pressure. Curiously, this is the opposite ordering to that observed in the supercritical Lennard–Jones system[44].

Thermodynamic anomalies. We have calculated a wide range of thermodynamic and electronic properties for potassium as a function of pressure. In all these, there is evidence of anomalous behaviour in the same pressure regime from 10 to 20 GPa over a wide temperature range, as shown in Fig. 1. We can interpret them in terms of a crossover from an atomic to an electride liquid (as outlined above), and corroborate this interpretation with analyses of the electronic properties (as described below).

Figure 2 shows thermal expansivity α, heat capacity C_{p}, speed of sound v_{s} and volume equation of state as a function of pressure. Expansivity α shows a strong dip in the crossover region, because crossing the transition line allows for more (compact) electride states to be occupied. The normal thermal expansion is still large enough to ensure positive α. Above 20 GPa, the occupation of electride states saturates, so this volume-reduction mechanism is no longer available. The heat capacity C_{p} is dominated by the Dulong–Petit $3R$ limit ($3R = 24.9$ J K^{-1} mol^{-1}, with R the ideal gas constant), but has an anomalous peak as a function of pressure at around 10 GPa. The electronic heat capacity exhibits a similar anomaly but with a reduced magnitude (Supplementary Note 7). For the speed of sound v_{s}, the change in compressibility (Supplementary Note 3) manifests here as a dip at around 18 GPa. The two-state thermodynamic model (Supplementary Note 3) was fitted to the machine-learned molecular dynamics (MLMD) data at 900 K to show the smooth oscillation in v_{s} with pressure. Equation of state $p(V)$ shows strong compressibility at low pressures—typical for alkali metals, while the inset reveals no measurable density discontinuity anywhere, just a subtle inflection at around 14 GPa.

Non-equilibrium property anomalies. Transport properties are non-equilibrium phenomena and therefore not directly associated with the Ehrenfest phase transition definitions. Nevertheless, when there are different structures, one can expect differences in the non-equilibrium properties.

Figure 3a shows anomalous diffusion behaviour, with a distinct plateau in the ionic diffusivity across the 10–20 GPa transition region. We can understand this as follows: in the electride, electrons move to interstitial locations such that some potassiums can be thought of as positively charged cations. Cations are smaller than neutral atoms and can therefore diffuse more easily. The increasing fraction of potassium cations across the transition region leads to enhanced diffusion, largely cancelling out the normal decrease due to reduced free volume. The diffusivity at various temperatures can be collapsed onto a unique curve, suggesting that diffusion is thermally activated, but the liquid structure is not strongly affected by temperature. No hysteresis or discontinuity in density was observed (Fig. 3b), further suggesting that there is no first-order liquid–liquid transition.

The diffusivity can be related to viscosity η via the Einstein–Stokes relation $D = \frac{k_{\mathrm{B}}T}{6\pi\,\eta\,r}$ with k_{B} the Boltzmann constant; however, this relation requires knowing the particle radius r, which is uncertain, since the ions are converting from neutral to cations. However, the MLMD enables us to calculate the viscosity from the Green–Kubo relations and fluctuations in the stress tensor, as shown in Fig. 3c. We then use this independent calculation of the viscosity

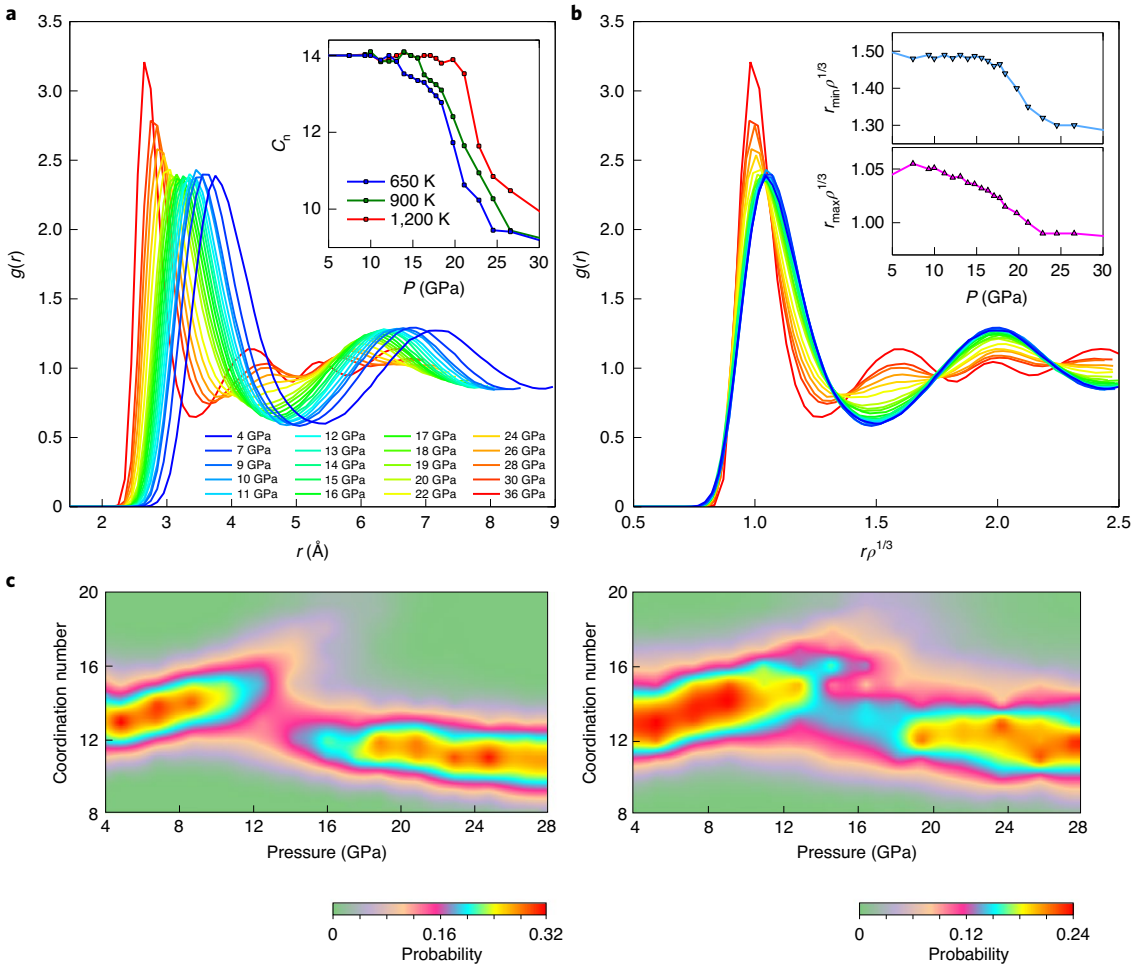

Fig. 4 | Structural properties of liquid potassium from AIMD simulations. a, RDFs at selected pressures and 650 K; inset shows the average coordination number C_n defined as the cumulative distribution integrated to the first minimum r_{min}. **b**, RDFs with distances scaled by particle density $\rho^{\frac{1}{3}}$, at the same pressures as shown in **a**; insets show the positions of the first maximum and minimum with respect to pressure (r_{max} and r_{min}). **c**, Heat map of distribution of coordination numbers C_n versus pressure at 650 K (left) and 1,200 K (right). Probability distribution of coordination numbers from MLMD, $p(C_n)$, versus pressure, at 650 K (left) and 1,200 K (right). $p(C_n)$ isevaluated at integer C_n, and then shown as a heat map. Colours show these probabilities, normalized at each pressure.

to invert the Einstein–Stokes relation and obtain an effective particle size (Fig. 3d), which drops sharply in the transition region. This effective size should not be taken as the average size, because it is weighted by its contribution to the diffusion. A sharp drop occurs at about 10 GPa, suggesting that a small number of small ions can strongly influence the diffusion behaviour.

Structural properties. The radial distribution function (RDF) is measurable by diffraction as the Fourier transform of the liquid structure factor. Figure 4a,b show that below 12 GPa, the RDF changes only by a scale factor. Above that pressure, the liquid has a very different structure. The first peak narrows and moves to a smaller radius—small even when the overall reduction in volume is factored out, which can be interpreted as the creation of smaller ions. In the normalized RDF, we see that the second neighbours are also much closer. These two effects drive the densification, despite the drop in near-neighbour coordination. Figure 4c clearly shows the transformation in terms of distributions of coordination number.

Electronic properties. Another potentially measurable quantity is reflectivity. This cannot be obtained from the classical potential, but we can calculate it using the electronic structure from the ab initio data. In Fig. 5a, we show the calculated reflectivity of liquid potassium at wavelength $\lambda = 532$ nm and several temperatures, compared with the solid phases. The crossover in reflectivity across the liquid transformation region is clear and follows the same trend as in the solid phases, though the dip is not as pronounced, and is virtually independent of temperature. A similar reduction in conductivity was observed in liquid lithium under pressure in experiments and simulations[45,46].

We use Bader analysis[47] to determine the electride nature of the system (Fig. 5b) by decomposing the charge density. Specifically, we study the distribution of non-nuclear Bader charges, q_{NN}, which is a measure for the electride fraction and strength of the electride sites. The number of q_{NN}, the integral of the distribution, rises strongly to about $x = 0.3$ electride sites per atom at around 12 GPa. The peaks of the distributions rise most dramatically between 12 and 20 GPa, where q_{NN} saturates at around 0.4e, close to the values of q_{NN} in phase IV (oP8) at 40 GPa and the guest electride channels in phase IIIa at 20 GPa. Counting charge within the basins of electron localization function (ELF)[48] rather than charge basins for solid IIIa[20] found that q_{NN} was higher by a factor of three, and this is also likely to be true for the liquid q_{NN} distribution.

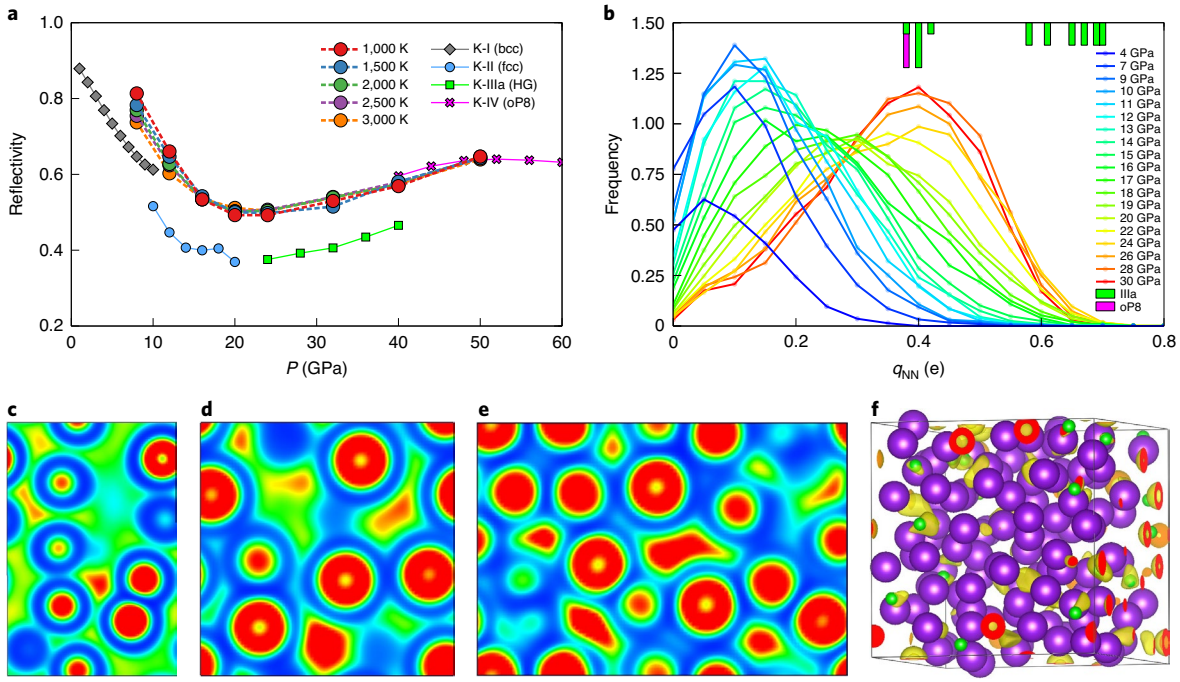

Fig. 5 | Electronic properties of liquid potassium. a, Reflectivity at 532 nm (green laser) based on the DFT calculations of AIMD snapshots and optimized solid phases. **b**, Distributions of non-nuclear charges, q_{NN}, for liquid potassium as a function of pressure (lines) at 650 K, and q_{NN} values for related solid electride phases are included above (bars): phase IIIa/oP8 at 20/40 GPa. **c**–**e**, ELF along typical (010) slices in simulation snapshots at 1,200 K and 2 GPa (**c**), 16 GPa (**d**) and 26 GPa (**e**). ELF values are shown in the RGB scale from 0 (blue) to 0.70 (red), with 0.35 (green). **f**, AIMD snapshots of potassium (purple), sites of q_{NN} (green) and ELF = 0.7 isosurfaces (yellow).

Figure 5c–e uses the ELF, which provides a clearer picture of the pressure-induced free electron to electride transitions. At 2 GPa, all the ELF maxima are nearly spherical, showing them to be associated with the potassium ions. In the transformation region, there are also non-nuclear ELF maxima (non-circular red blobs) associated with the electride pseudo-anions. By 26 GPa, these non-nuclear maxima are even more prevalent. Figure 5f and Supplementary Video 1 relate the Bader and ELF analyses, showing that the q_{NN} values are associated with regions of localized electrons, that is, high values of ELF.

Discussion and conclusions. We have simulated the behaviour of high-pressure liquid potassium using molecular dynamics with interactions derived from both density functional theory (DFT) calculations and a machine-learned potential. The simulations show anomalous behaviours in a wide range of properties between 10 and 20 GPa. However, we do not see any hysteresis or density discontinuity. These observations led us to propose that liquid potassium exhibits a gradual increase in electride content. The electride/ionic potassium ions generally have higher energy than atomic potassium, but on mixing, they occupy a smaller volume. This transformation is primarily driven by pressure, so the lines tracing the peaks of anomalous behaviours are nearly vertical on the pressure–temperature phase diagram (Fig. 1).

This crossover behaviour can be modelled as a two-state system, in which the 'electride' state has higher energy than the atomic state. These simple two-state models predict that anomalies in C_p, α and v_s occur in that sequence with pressure—just as observed in the simulations here. In these models, the excess heat capacity comes from the extra degree of freedom offered by 'ionization', the reduced thermal expansion is due to thermal excitation into the (denser) electride state and the excess compressibility comes from the additional compression mechanism offered by creating the electride.

From the anomalies in the sound velocity and thermal expansion, in the two-state thermodynamic model, we obtain $\Delta V/V = 0.05$ and $\Delta S = -0.2R$ between the atomic and electride states, which gives a negative, almost vertical slope of $-500\,\mathrm{K\,GPa^{-1}}$ for the boundary between the two unmixed states, in agreement with the vertical slope marking the observed anomalies (Fig. 1). Notice that a negative slope is required by the observation that the denser electride state is obtained by heating the liquid at a constant pressure.

The diffusion plateau can be understood by smaller 'ions' moving more quickly. The distinctive change in the local structure can be seen in the radial distribution and coordination. The conductivity/reflectivity shows a crossover with pressure that mirrors the transition from nearly free electron metal to electride phases in the solid.

The low-pressure liquid is extremely compressible with no characteristic ionic radius, as the nearest-neighbour distance scales with the volume. At high pressure, the interionic spacing approaches twice the ionic radius of 1.3 Å. The coordination number drop (Fig. 4c) is consistent with the transition from close-packed solid (coordination number $C_n = 12$) to the incommensurate electride phase of the host–guest (HG) structure ($C_n = 9$). The electride-containing phase is denser, despite the lower coordination, because the near neighbours are closer together and the second neighbour shell is much closer. The liquid becomes denser than the solid after the melting maxima at around 10 GPa, implying that the dense liquid takes on the properties of the phases succeeding face-centred cubic (fcc). Solid phases of HG structures and phase IV (oP8) were observed as moderate electrides[20,49].

In conclusion, we have shown that potassium becomes a type of two-component liquid in which atomic and ionic/electride potassium coexist. The phase diagram for potassium is similar to other alkali metals, and we can expect that this type of two-component liquid will be a general feature. Our work resolves the mystery of

the negative Clapeyron slope between phase II (fcc) and liquid: the negative slope means that the liquid is denser than the solid. This cannot be due to more efficient packing, because fcc is the most efficient packing possible for spheres. Here the cause is revealed as the larger electride fraction in the liquid, where the ions are smaller than the atoms, and electrons can adopt any shape to fit into the interstitial region where they are located.

Online content

Any methods, additional references, Nature Research reporting summaries, source data, extended data, supplementary information, acknowledgements, peer review information; details of author contributions and competing interests; and statements of data and code availability are available at https://doi.org/10.1038/s41567-021-01244-w.

Received: 13 May 2020; Accepted: 9 April 2021;
Published online: 17 May 2021

References

1. Katayama, Y. et al. A first-order liquid–liquid phase transition in phosphorus. *Nature* **403**, 170–173 (2000).
2. Ashcroft, N. The hydrogen liquids. *J. Phys. Condens. Matter* **12**, A129 (2000).
3. Knudson, M. D. et al. Direct observation of an abrupt insulator-to-metal transition in dense liquid deuterium. *Science* **348**, 1455–1460 (2015).
4. McMahon, J. M., Morales, M. A., Pierleoni, C. & Ceperley, D. M. The properties of hydrogen and helium under extreme conditions. *Rev. Mod. Phys.* **84**, 1607 (2012).
5. Geng, H. Y., Wu, Q., Marqués, M. & Ackland, G. J. Thermodynamic anomalies and three distinct liquid-liquid transitions in warm dense liquid hydrogen. *Phys. Rev. B* **100**, 134109 (2019).
6. London, F. The λ-phenomenon of liquid helium and the Bose–Einstein degeneracy. *Nature* **141**, 643–644 (1938).
7. Mishima, O. & Stanley, H. E. The relationship between liquid, supercooled and glassy water. *Nature* **396**, 329–335 (1998).
8. Soper, A. K. & Ricci, M. A. Structures of high-density and low-density water. *Phys. Rev. Lett.* **84**, 2881 (2000).
9. Strässle, T. et al. Structure of dense liquid water by neutron scattering to 6.5 GPa and 670 K. *Phys. Rev. Lett.* **96**, 067801 (2006).
10. Fanetti, S. et al. Structure and dynamics of low-density and high-density liquid water at high pressure. *J. Phys. Chem. Lett.* **5**, 235–240 (2014).
11. Lapini, A. et al. Pressure dependence of hydrogen-bond dynamics in liquid water probed by ultrafast infrared spectroscopy. *J. Phys. Chem. Lett.* **7**, 3579–3584 (2016).
12. Bove, L. E. et al. Translational and rotational diffusion in water in the gigapascal range. *Phys. Rev. Lett.* **111**, 185901 (2013).
13. Cadien, A. et al. First-order liquid-liquid phase transition in cerium. *Phys. Rev. Lett.* **110**, 125503 (2013).
14. Nomura, R. et al. Spin crossover and iron-rich silicate melt in the Earth's deep mantle. *Nature* **473**, 199–202 (2011).
15. Ramo, D. M. & Stixrude, L. Spin crossover in Fe_2SiO_4 liquid at high pressure. *Geophys. Res. Lett.* **41**, 4512–4518 (2014).
16. Gregoryanz, E., Degtyareva, O., Somayazulu, M., Hemley, R. & Mao, H.-K. Melting of dense sodium. *Phys. Rev. Lett.* **94**, 185502 (2005).
17. Ma, Y. et al. Transparent dense sodium. *Nature* **458**, 182–185 (2009).
18. Guillaume, C. L. et al. Cold melting and solid structures of dense lithium. *Nat. Phys.* **7**, 211–214 (2011).
19. Narygina, O., McBride, E. E., Stinton, G. W. & McMahon, M. I. Melting curve of potassium to 22 GPa. *Phys. Rev. B* **84**, 054111 (2011).
20. Woolman, G. et al. Structural and electronic properties of the alkali metal incommensurate phases. *Phys. Rev. Mater.* **2**, 053604 (2018).
21. Dawes, S. B., Ward, D. L., Huang, R. H. & Dye, J. L. First electride crystal structure. *J. Am. Chem. Soc.* **108**, 3534–3535 (1986).
22. Dye, J. L. Electrides: ionic salts with electrons as the anions. *Science* **247**, 663–668 (1990).
23. Miyakawa, M. et al. Superconductivity in an inorganic electride $12CaO{\cdot}7Al_2O_3{:}e^-$. *J. Am. Chem. Soc.* **129**, 7270–7271 (2007).
24. Sushko, P. V., Shluger, A. L., Hirano, M. & Hosono, H. From insulator to electride: a theoretical model of nanoporous oxide $12CaO{\cdot}7Al_2O_3$. *J. Am. Chem. Soc.* **129**, 942–951 (2007).
25. Kitano, M. et al. Ammonia synthesis using a stable electride as an electron donor and reversible hydrogen store. *Nat. Chem.* **4**, 934–940 (2012).
26. Kitano, M. et al. Electride support boosts nitrogen dissociation over ruthenium catalyst and shifts the bottleneck in ammonia synthesis. *Nat. Commun.* **6**, 6731 (2015).
27. Zhang, Y., Wang, H., Wang, Y., Zhang, L. & Ma, Y. Computer-assisted inverse design of inorganic electrides. *Phys. Rev. X* **7**, 011017 (2017).
28. Tsujia, K., Katayama, Y., Morimoto, Y. & Shimomura, O. Structure of liquid rubidium under high pressure. *J. Non Cryst. Solids* **205-207**, 295–298 (1996).
29. Gorelli, F. A. et al. Simple-to-complex transformation in liquid rubidium. *J. Phys. Chem. Lett.* **9**, 2909–2913 (2018).
30. Tsuji, K. et al. Pressure-induced structural change of liquid cesium. *J. Non Cryst. Solids* **117–118**, 72–75 (1990).
31. Falconi, S., Lundegaard, L. F., Hejny, C. & McMahon, M. I. X-ray diffraction study of liquid Cs up to 9.8 GPa. *Phys. Rev. Lett.* **94**, 125507 (2005).
32. Hattori, T. Is there a pressure-induced discontinuous volume change in liquid Cs? *Phys. Rev. B* **97**, 100101 (2018).
33. Decremps, F. et al. Sound velocity and equation of state in liquid cesium at high pressure and high temperature. *Phys. Rev. B* **98**, 184103 (2018).
34. Tamblyn, I., Raty, J.-Y. & Bonev, S. A. Tetrahedral clustering in molten lithium under pressure. *Phys. Rev. Lett.* **101**, 075703 (2008).
35. Raty, J.-Y., Schwegler, E. & Bonev, S. A. Electronic and structural transitions in dense liquid sodium. *Nature* **449**, 448–451 (2007).
36. Bryk, T. et al. Dynamical crossover at the liquid-liquid transformation of a compressed molten alkali metal. *Phys. Rev. Lett.* **111**, 077801 (2013).
37. Falconi, S. & Ackland, G. J. Ab initio simulations in liquid caesium at high pressure and temperature. *Phys. Rev. B* **73**, 184204 (2006).
38. Boates, B. *On the Stability of sp-Valent Materials at High Pressure*. PhD thesis, Dalhousie Univ. (2013).
39. Zhao, L., Zong, H., Ding, X., Sun, J. & Ackland, G. J. Commensurate-incommensurate phase transition of dense potassium simulated by machine-learned interatomic potential. *Phys. Rev. B* **100**, 220101 (2019).
40. Robinson, V. N., Zong, H., Ackland, G. J., Woolman, G. & Hermann, A. On the chain-melted phase of matter. *Proc. Natl Acad. Sci. USA* **116**, 10297–10302 (2019).
41. Rapoport, E. Model for melting-curve maxima at high pressure. *J. Chem. Phys.* **46**, 2891–2895 (1967).
42. Tanaka, H. Bond orientational order in liquids: towards a unified description of water-like anomalies, liquid-liquid transition, glass transition, and crystallization. *Eur. Phys. J. E* **35**, 113 (2012).
43. Holten, V. & Anisimov, M. A. Entropy-driven liquid–liquid separation in supercooled water. *Sci. Rep.* **2**, 713 (2012).
44. Brazhkin, V. V., Fomin, Y. D., Lyapin, A. G., Ryzhov, V. N. & Tsiok, E. N. Widom line for the liquid–gas transition in Lennard–Jones system. *J. Phys. Chem. B* **115**, 14112–14115 (2011).
45. Bastea, M. & Bastea, S. Electrical conductivity of lithium at megabar pressures. *Phys. Rev. B* **65**, 193104 (2002).
46. Kietzmann, A., Redmer, R., Desjarlais, M. P. & Mattsson, T. R. Complex behavior of fluid lithium under extreme conditions. *Phys. Rev. Lett.* **101**, 070401 (2008).
47. Bader, R. F. W. *Atoms in Molecules: A Quantum Theory* (Oxford Univ. Press, 1994).
48. Savin, A. et al. Electron localization in solid-state structures of the elements: the diamond structure. *Angew. Chem. Int. Ed.* **31**, 187–188 (1992).
49. Marqués, M. et al. Potassium under pressure: a pseudobinary ionic compound. *Phys. Rev. Lett.* **103**, 115501 (2009).
50. McBride, E. E. et al. One-dimensional chain melting in incommensurate potassium. *Phys. Rev. B* **91**, 144111 (2015).

Methods

AIMD. DFT calculations utilized the CASTEP code[51]. We used the generalized gradient approximation exchange–correlation functional[52] and a 9e ultrasoft pseudopotential with 1.7 Bohr inner-core radius and 400 eV plane-wave cutoff with k points sampled at the Γ point only for AIMD, and with a grid density of 0.02 Å^{-1} for structure optimization. Forces are calculated using the Hellmann–Feynman theorem.

Simulations ran at a fixed density (NVT) with a Nosé–Hoover thermostat using a timestep of 0.75 fs, Gaussian smearing of 0.1 eV and sampling of up to 25 ps. Additional simulations were performed at fixed pressure (NPT) and all observables of the electride transition are consistent. The initial conditions for the liquid state for the 650 K isotherm were attained by quenching a 1,000 K melt of 128 bcc potassium ions. For the 1,500 K isotherm, the simulations ranged from 108 to 250 potassium ions from melting the stable solid phases of bcc, fcc and IIIa at various pressures.

Analysing the non-nuclear charge was performed using the Bader partitioning scheme[47] for the charge density. For a particular pressure, 100 snapshots were selected for charge density and ELF calculations. Most Bader charges were found close to potassium ions (0.4 Å), while we deem non-nuclear charges, q_{NN}, as those that were found far away (2.0 Å) from the potassium ions. These distances are consistent with the ion–ion interstitial $g(r)$ regions, and the ion–q_{NN} $g(r)$ region shows clear peaks in the minima of the ion–ion $g(r)$ regions. The majority of q_{NN} found with either Bader and ELF were found in similar positions, with some differences as expected, and may underestimate the total amount of non-nuclear localized electrons.

Reflectivity. The interband dielectric function $\varepsilon(\omega)$ was determined within the random phase approximation using CASTEP and its OptaDOS extension[53], with dense k-point grids for all solid phases and (8,8,8) grids for AIMD snapshots of 108 atoms. An intraband contribution $\varepsilon^{\text{intra}}(\omega)$ was added using a Drude term with 100 THz broadening. Four snapshots per AIMD trajectory were sufficient to converge the spectral features of the dielectric function. The reflectivity was then determined using the usual expressions[53].

Machine-learning interatomic potential. We used a domain-knowledge-based machine learning approach to match the true potential energy surface of potassium[39,40]. Here the machine-learning interatomic potential (MLIP) is directly learned from an accurate reference database of first-principles calculations[54] using the Vienna Ab initio Simulation Package (VASP) code[55]. To capture the different phases in the temperature–pressure phase diagram of potassium, more than 20,000 initial reference configurations were accumulated from the AIMD simulations of different stable phases and their melts. The local chemical environment of these reference configurations were then fingerprinted by some atom-centred symmetry function descriptors (or fingerprints). These descriptors are mapped into the corresponding atomic energy/forces with the kernel ridge regression method. The MLIP was further optimized by an iterative scheme, in which the potential is fitted to the existing reference database, and then simulations with the potential are run to create a more diverse set of structures. This way, the MLIP 'steers' itself into regions of configuration space that need to be further explored. Additional information and benchmarks about the MLIP can be found in Supplementary Note 1 as well as our recent work[39].

The AIMD database includes Hellmann–Feynman forces that are calculated in VASP[55] as the derivatives of the generalized free energy. Consequently, the electronic entropy is included in both AIMD and MLMD forces; this is expected to be a small effect[56,57]. We used a fixed Gaussian smearing of 0.2 eV in all AIMD runs. In Supplementary Note 8, we show that the resulting forces deviate from those obtained with temperature-adjusted Fermi–Dirac smearing by only around 10 meV Å^{-1}. We note that this value is less than the uncertainty of the MLIP. However, electronic entropy can add a notable contribution to the heat capacity[58], which we calculate separately from the electronic density of states using the Sommerfeld approximation (Supplementary Fig. 18).

Classic molecular dynamics simulations were then performed using a timestep of 1 fs, and periodic boundary conditions were applied along all three dimensions. The Nosé–Hoover thermostat and Parrinello–Rahman barostat[59,60] were used for controlling the temperature and pressure, respectively. All simulations were carried out using the LAMMPS package, and the atomic configurations were visualized with the AtomEye package. Typical models of potassium liquid containing 3,456 atoms were obtained by heating a single crystal at 2,000 K and specific pressures, and these liquid structures are used to study the corresponding properties of the liquid (such as diffusivity, heat capacity and speed of sound) at selected temperatures and pressures.

Data availability

All the data presented in Figs. 1–5 are available as source data. All other data that support the plots within this paper and other findings of this study are available from the corresponding authors upon reasonable request.

Code availability

Code is available at https://github.com/zhaolongxjtu/KMLP.

References

51. Clark, S. J. et al. First principles methods using CASTEP. *Z. Krist.* **220**, 567–570 (2005).
52. Perdew, J. P., Burke, K. & Ernzerhof, M. Generalized gradient approximation made simple. *Phys. Rev. Lett.* **77**, 3865 (1996).
53. Morris, A. J., Nicholls, R. J., Pickard, C. J. & Yates, J. R. OptaDOS: a tool for obtaining density of states, core-level and optical spectra from electronic structure codes. *Comput. Phys. Commun.* **185**, 1477–1485 (2014).
54. Kresse, G. & Furthmüller, J. Efficiency of ab-initio total energy calculations for metals and semiconductors using a plane-wave basis set. *Comput. Mater. Sci.* **6**, 15–50 (1996).
55. Kresse, G. & Furthmüller, J. Efficient iterative schemes for ab initio total-energy calculations using a plane-wave basis set. *Phys. Rev. B* **54**, 11169–11186 (1996).
56. Ackland, G. J. Temperature dependence in interatomic potentials and an improved potential for Ti. *J. Phys. Conf. Ser.* **402**, 012001 (2012).
57. Khakshouri, S., Alfè, D. & Duffy, D. M. Development of an electron-temperature-dependent interatomic potential for molecular dynamics simulation of tungsten under electronic excitation. *Phys. Rev. B* **78**, 224304 (2008).
58. Zhang, X., Grabowski, B., Körmann, F., Freysoldt, C. & Neugebauer, J. Accurate electronic free energies of the 3*d*, 4*d*, and 5*d* transition metals at high temperatures. *Phys. Rev. B* **95**, 165126 (2017).
59. Nosé, S. A unified formulation of the constant temperature molecular dynamics methods. *J. Phys. Chem. A* **81**, 511–519 (1984).
60. Parrinello, M. & Rahman, A. Polymorphic transitions in single crystals: a new molecular dynamics method. *J. Appl. Phys.* **52**, 7182 (1981).

Acknowledgements

H.Z. and G.J.A. acknowledge the ERC project HECATE for funding. V.N.R. thanks the UK's EPSRC for CM-CDT studentships. H.Z. and X.D. thank the National Natural Science Foundation of China (51931004 and 51871177) and the 111 project 2.0 (BP2018008). We are grateful for computational support from the UK national high performance computing service (ARCHER) and the UK Materials and Molecular Modelling Hub, which is partially funded by EPSRC (EP/P020194), access for both of which was obtained via the UKCP consortium and funded by EPSRC grant no. EP/P022561/1.

Author contributions

H.Z., V.N.R., A.H. and G.J.A. conceived the research. H.Z., V.N.R., A.H. and L.Z. conducted the simulation. S.S. and G.J.A. created the two-state liquid model. All the authors participated in the analysis and interpretation of the results as well as writing of the manuscript.

Competing interests

The authors declare no competing interests.

Additional information

Supplementary information The online version contains supplementary material available at https://doi.org/10.1038/s41567-021-01244-w.

Correspondence and requests for materials should be addressed to L.Z. or G.J.A.

Peer review information *Nature Physics* thanks Takanori Hattori, Artem Oganov and the other, anonymous, reviewer(s) for their contribution to the peer review of this work.

Reprints and permissions information is available at www.nature.com/reprints.